Annals of Nuclear Energy 213 (2025) 111125

Contents lists available at ScienceDirect

Annals of Nuclear Energy

journal homepage: www.elsevier.com/locate/anucene

Coolant contamination in gas-cooled reactors due to neutronic sputtering

P. Chiovaro [a,*], L. Girard [b], A. Quartararo [a], S. Basile [a], G. Bongiovì [a], P.A. Di Maio [a], I. Moscato [a,c], E. Vallone [a], G. Zhou [d]

[a] Department of Engineering, University of Palermo, Viale delle Scienze Ed. 6, 90128, Palermo, Italy
[b] École Nationale Supérieure d'Ingénieurs de Caen, 6, Boulevard Maréchal Juin, 14000, Caen, Normandie, France
[c] Fusion Technology Department – Programme Management Unit, EUROfusion Consortium, Boltzmannstraße 2, 85748, Garching, Germany
[d] Institute for Neutron Physics and Reactor Technology (INR), Karlsruhe Institute of Technology (KIT), Hermann-von-Helmholtz-Platz 1, 76344, Eggenstein-Leopoldshafen, Germany

ARTICLE INFO

Keywords:
Neutron sputtering
Coolant contamination
Gas-cooled reactors
DEMO HCPB

ABSTRACT

The transport of activated material beyond the bio-shields of nuclear reactors creates a gamma radiation field that poses a risk to operating, maintenance and inspection personnel. This makes the presence of activated material in the primary heat transfer system a critical safety and environmental concern. Neutron sputtering, a phenomenon that occurs when energetic neutrons collide with structural material and cause atoms to be ejected from the surface adjacent to cooling channels or tubes, is the primary mechanism in gas-cooled reactors that contributes to the inventory of activated material within the loops. The idea behind the work is centered on the evaluation of the recoil ranges of the daughter nuclei, therefore the study aims to investigate the physics behind the phenomenology considered in order to develop a suitable method to obtain quantitative results that can be used in the design of gas-cooled nuclear reactors.

1. Introduction

In nuclear reactors the presence of activated material in the Primary Heat Transport System (PHTS) is a key safety and environmental issue as it is transported beyond the bio-shields inducing a gamma radiation field that is hazardous to the inspection, maintenance, and operating staff (IAEA, 2012). In addition, activation products in the coolant circuits must be considered in accidental scenarios involving some break in the loop. In gas cooled fission and fusion reactors, the main mechanism contributing to the Activated Coolant Material (ACM) inventories within the loops is the neutron sputtering (Brassert et al., 1959; Bickford, 1980; Behrisch, 1983; Karditsas and Forty, 1997). This phenomenon occurs when energetic neutrons collide with the structural material, causing atoms to be ejected from the surface neighboring cooling channels or tubes. As these ejected atoms accumulate, they can redeposit on cooler surfaces within the loop or react with other elements, leading to a build-up of materials. This accumulation not only affects the efficiency of heat transfer and cooling capabilities of the gas loops, but also poses challenges in maintaining the purity of the cooling gas. The sputtered material can also change the chemical composition and mechanical properties of the structural material, potentially leading to corrosion or other forms of degradation. Managing this inventory accumulation is crucial to ensure the long-term integrity of the reactor cooling system and its safety. This phenomenon is even more intense the harder the neutron spectrum, both because many radioisotopes are produced in threshold reactions and for the energy imparted to the recoil nucleus, which is why it is particularly relevant in helium-cooled fusion reactors (Klein and Vogelsang, 1985; Ye et al., 2001; Harling et al., 1976; Kaminsky and Das, 1976; Ye et al., 1997; Bang-jiao et al., 1999).

This paper presents a study regarding the assessment of the flow rate of activated nuclei sputtered in the coolant circuits during nuclear reactor operation. The underlying idea of the paper is focused on the evaluation of daughter nucleus recoil ranges in neutronic reactions, and it takes its initial cue from the work shown in Karditsas and Forty (1997), Forty and Kardistas (1994), so the study aims at investigating the physics behind the phenomenology considered in such a way to develop a proper method to get quantitative results to be used in the design of gas-cooled nuclear reactors. The method developed was then used for a preliminary rough determination of ACM inventories and assessment of their mass flow rates in the DEMO fusion reactor (Federici et al., 2019, 2021) helium cooling loop, namely the Helium-Cooled Pebble Bed (HCPB) breeding blanket PHTS (Zhou et al., 2023) by adopting a sub-modeling approach. Of course, this ACM inventories assessment represents a starting point for more refined

* Corresponding author.
E-mail address: pierluigi.chiovaro@unipa.it (P. Chiovaro).

https://doi.org/10.1016/j.anucene.2024.111125
Received 18 September 2024; Received in revised form 14 November 2024; Accepted 4 December 2024
Available online 21 December 2024

neutronic calculations and for transport analysis to determine a map of the radioisotope concentrations along the hydraulic circuit of the HCPB blanket concept.

A description of the problem addressed, the theoretical method adopted, and the physical quantities of interest are provided in Section 2. Section 3 deals with the numerical implementation of the developed method focusing on the DEMO HCPB blanket, which is briefly described, then results are shown and commented.

2. Theory

The sputtering phenomenon leading to gas contamination is associated with the capture, in the structural material that makes up the cooling circuit, of a neutron at a given speed by a nucleus that is assumed to be stationary in the laboratory reference system. The compound nucleus decays rapidly in a time interval between 10^{-20} to 10^{-14} seconds (Blin-Stoyle, 1991) so traveling a very small distance in the direction of the incident neutron, due to conservation of momentum. Thus, the compound nucleus decays into one or more energetic particles of low mass also giving the residual daughter nucleus enough recoil energy to push it through the lattice. It is noted that both the low mass particles and the daughter's angular distributions are typically forward biased with respect to the incident neutron direction (Forty and Kardistas, 1994). Obviously, only recoil nuclei produced at a distance from the channel or tube wetted surfaces lower or equal to their traveling range have a non-zero probability of reaching the coolant.

2.1. Recoil nucleus range

In order to calculate some average values for the recoil nucleus path range R of each reaction considered, below we derive an analytical expression for it.

As in numerous previous works on diverse subjects e.g. Forty and Kardistas (1994), Salvat (2022), Grimes et al. (2017) the stopping power formula (Bethe and Heitler, 1934) was employed:

$$-\frac{\mathrm{d}E}{\mathrm{d}x}=\frac{z^2e^4\rho N_A Z}{4\pi\varepsilon_0^2 m_e V^2 A}\ln\left(\frac{2m_eV^2}{B}\right) \tag{1}$$

Where z is the average effective charge number of the daughter atom along its path (Forty and Kardistas, 1994); e is the elementary charge; ρ is the mass density of the lattice; N_A is the Avogadro's number; Z the effective atomic number of the lattice; ϵ_0 is the vacuum permittivity; m_e is the electron mass; V is the velocity of the daughter nucleus; B is the average binding energy of electrons in the lattice (Forty and Kardistas, 1994).

It is observed that Eq. (1) was solved in the domain of the energy of the recoil nucleus rather than in the speed domain, using the formula:

$$E=\frac{1}{2}m_{\mathrm{D}}V^2 \tag{2}$$

Where m_{D} is the mass of the daughter nucleus.

So that it holds that:

$$-\frac{\mathrm{d}E}{\mathrm{d}x}=\frac{f_1}{E}\ln\left(f_2E\right) \tag{3}$$

Where:

$$f_1=\frac{m_{\mathrm{D}}}{2}\frac{z^2e^4\rho N_a Z}{4\pi\varepsilon_0^2 m_e A} \tag{4}$$

$$f_2=\frac{2}{m_{\mathrm{D}}}\frac{2m_e}{B} \tag{5}$$

From Eq. (3) the following equation springs:

$$\int_0^R\mathrm{d}x=\frac{1}{f_1}\int_{E_{\mathrm{D}}}^0\frac{E}{\ln\left(f_2E\right)}\mathrm{d}E \tag{6}$$

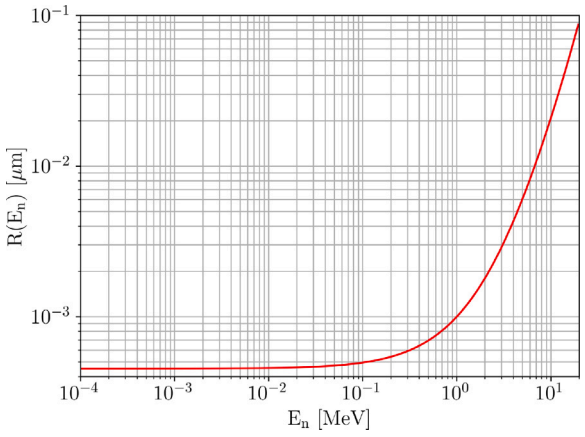

Fig. 1. Energy profile of R for ^{55}Fe originated from ^{58}Ni(n, α)^{55}Fe.

In which the E_{D} is an average recoil nucleus initial energy to be assessed. It is worth noting that the integration on the right-hand side of Eq. (6) is not strictly valid in the low energy limit, but for practical tasks it is useful to calculate range differences (Salvat, 2022; Evans, 1955).

It is easy to show that (see Appendix A):

$$R\left(E_{\mathrm{D}}\right)=\frac{1}{f_1f_2^2}\mathrm{E}_1\left[-2\ln\left(f_2E_{\mathrm{D}}\right)\right] \tag{7}$$

Where E_1 is the exponential–integral function (Abramowitz and Stegun, 1965). The quantity R is a function of E_{D}, which in turn is a function of the incident neutron energy, it can be shown that (see Appendix B):

$$E_{\mathrm{D}}=AE_n+C \tag{8}$$

Where E_n is neutron energy while A and C are constants depending on the masses and the Q-value of the reaction.

It is important to note that in the following, both the average E_{D} and the maximum energy $E_{\mathrm{D_{lim}}}$ of the recoil nucleus will be taken into account. R can therefore take the following functional form:

$$R\left(E_n\right)=\frac{1}{f_1f_2^2}\mathrm{E}_1\left\{-2\ln\left[f_2\left(AE_n+C\right)\right]\right\} \tag{9}$$

It should be noted that the domain of the function R is defined by the relation $E_n>-\frac{C}{A}=-cQ$ (see Appendix B) where c is a positive constant and Q, the Q-value of the reaction. So, for exothermic reactions the domain of R is $(0,+\infty)$ while for endothermic reactions it is $(c\left|Q\right|,+\infty)$.

Fig. 1 shows in a double-logarithmic scale the profile of R versus E_n for the reaction ^{58}Ni(n, α)^{55}Fe which is exothermic, and highlights how such a law is a monotonic growing function.

With the help of Eq. (9), it is possible to calculate different types of averages for R in such a way as to have a better understanding of the method to be selected for calculating the number of activated nuclei entering the coolant flow.

These averages in question differ to one another according to the probability density function (pdf) considered. For sake of simplicity E_n will be denoted by E from now on. Three pdfs, $p_i\left(E\right)$ with $i=1,2,3$ have been selected:

$$p_1\left(E\right)=\frac{\int_V\Sigma_{X(n,b)D}\left(\underline{r},E\right)\varphi\left(\underline{r},E\right)\mathrm{d}V'}{\int_0^{+\infty}\int_V\Sigma_{X(n,b)D}\left(\underline{r},E\right)\varphi\left(\underline{r},E\right)\mathrm{d}V'\mathrm{d}E} \tag{10}$$

In which the weighting function is the production rate of the recoil nucleus. Σ and φ are the macroscopic cross section of the neutron reaction X(n,b)D and the energy density of the neutron flux respectively.

$$p_2(E) = \frac{\int_V \varphi(\underline{r}, E)\,\mathrm{d}V'}{\int_0^{+\infty}\int_V \varphi(\underline{r}, E)\,\mathrm{d}V'\mathrm{d}E} \tag{11}$$

In which the weighting function is the energy density of the neutron flux.

$$p_3(E) = \frac{\int_V n(\underline{r}, E)\,\mathrm{d}V'}{\int_0^{+\infty}\int_V n(\underline{r}, E)\,\mathrm{d}V'\mathrm{d}E} \tag{12}$$

In which the weighting function is the volumetric density of the neutron population n.

Therefore, the three averages of R taken into account are the following:

$$\begin{aligned} R_1 &= \int_0^{+\infty} R(E)\,p_1(E)\,\mathrm{d}E, \\ R_2 &= \int_0^{+\infty} R(E)\,p_2(E)\,\mathrm{d}E \quad \text{and} \\ R_3 &= \int_0^{+\infty} R(E)\,p_3(E)\,\mathrm{d}E \end{aligned} \tag{13}$$

Moreover, also the next three values for R were considered:

$$R_4 = R(E_1), \quad R_5 = R(E_2) \quad \text{and} \quad R_6 = R(E_3) \tag{14}$$

Where E_i, with $i = 1,2,3$ are averages energies defined in the following way:

$$\begin{aligned} E_1 &= \int_0^{+\infty} E p_1(E)\,\mathrm{d}E, \\ E_2 &= \int_0^{+\infty} E p_2(E)\,\mathrm{d}E \quad \text{and} \\ E_3 &= \int_0^{+\infty} E p_3(E)\,\mathrm{d}E \end{aligned} \tag{15}$$

Also, the value of R related to $E_{\mathrm{D_{lim}}}$ is evaluated:

$$R_7 = R\left(E_{\mathrm{D_{lim}}}\right) \tag{16}$$

As far as $E_{\mathrm{D_{lim}}}$ is concerned, it is a somewhat artificial quantity equal to the average neutron source energy, that is $E_{\mathrm{D_{lim}}}$=14.1 MeV, it was chosen to provide a sort of limiting R-value. In fact, such a value has been chosen because the numerical implementation of the developed method is carried out in a fusion-relevant nuclear system where the neutron energy source distribution is a Gaussian spectrum with a narrow width centered at 14.1 MeV in the case of deuterium–tritium fusion reactions.

Comparison among different values can provide important information about the physics of the problem and then suggest the best way to overcome it. The comparison between R_1 and R_2 can give an idea of how the cross section acts as a filter, especially when threshold reactions are involved. While the comparison between R_2 and R_3 can shed light on the effect of the spectrum in defining this quantity. The usefulness of the otherwise defined R_s will soon become clear in the following.

2.2. Assessment of the ACM flow rates towards the coolant

In this section, the various quantities introduced are accompanied by an indication of their physical dimensions, in order to make the subject under discussion as clear as possible. If q [t^{-1}] is the given isotope production rate in the volume, V_{eff} [l^3], which is the volume of the structural material around the channel/tube in the range $0 - R$, the related ACM flux rate q'' [$\mathrm{l}^{-2}\,\mathrm{t}^{-1}$] towards the coolant can be calculated as $q'' \approx P \cdot q/S_w$, where P is the probability that the recoil nucleus travels in the direction of the coolant and S_w [l^2] is the surface wetted by the coolant. q can be approximated as $q \approx Q \cdot V_{\mathrm{eff}}/V_{\mathrm{tot}}$, where Q [t^{-1}] is the given isotope production rate in the whole cell in which channels or tubes are located and V_{tot} [l^3] is its volume. As R is very small then $V_{\mathrm{eff}} \approx S_w \cdot R$, then it holds that $q'' \approx Q''' \cdot P \cdot R$, where Q''' [$\mathrm{l}^{-3}\mathrm{t}^{-1}$] is the volumetric density of the isotope production rate. Such quantities are related to one another by the following chain of equalities:

$$\begin{aligned} q'' \approx P \cdot \frac{q}{S_w} \approx P \cdot \frac{Q}{V_{tot}} \cdot \frac{V_{eff}}{S_w} \approx \\ P \cdot Q''' \cdot \frac{S_w \cdot R}{S_w} = Q''' \cdot P \cdot R \end{aligned} \tag{17}$$

It is observed that the quantity q'' is also useful to determine the mass flow rate G [$\mathrm{m}\,\mathrm{t}^{-1}$] of ACM to the coolant.

As far as P is concerned, considering the flatness of the surfaces of both the channels (usually with a square section) and the pipes (whose curvature is much greater than the recoil nucleus range), it is easy (Karditsas and Forty, 1997) to show that it is equal to 1/4. The quantity $P \cdot R$ can therefore be thought of as the distance to the surface within which each reaction produces a recoil nucleus that reaches the coolant.

3. Neutronic analysis

The numerical implementation of the theory described above has been developed for the breeding blanket of the DEMO nuclear fusion reactor, taking into account the design that foresees the so called HCPB blanket, the outline of which is given in the following paragraph. Neutronic analyses were performed by the Monte Carlo method adopting MCNP5.1.6 code (X-5 Monte Carlo Team, 2003) along with the JEFF 3.3 cross section library (NEA, 2017). In this respect, the reactions taken into account for the calculation are reported in Table 1.

These reactions have been selected on the basis of the past experience in the fusion field (Terranova and Di Pace, 2021) and in the nuclear power plants (National Research Council, 1996; Neeb, 1997). The half-lives of the radioactive recoil nuclei above introduced are summarized in Table 2 (Firestone, 1999).

It should be noted that radiative capture reactions have been neglected because (due to the very hard neutron spectrum in the HCPB blanket structural material) their production rate is much lower than reactions that produce both charged and uncharged particles, up to three orders of magnitude. In addition, the (n, γ) recoil particle energies are small (<1 KeV) (Sigmund, 1969) and so the distance they can travel in the lattice is rather modest.

3.1. DEMO HCPB blanket

In this paragraph, a brief outline of the blanket is drawn but an exhaustive description, with further information on the technology employed, can be found in Zhou et al. (2023).

The DEMO blanket is articulated in 16 sectors in the toroidal direction, each sector is made up of single modules with a poloidal extension, every sector is composed of two inboard segments and three outboard segments. Such single modules are built using straight poloidal First Wall (FW) panels with a toroidal rooftop shape and Breeding Zone (BZ) modules. In the specific case of HCPB blanket, the resulting section has a high degree of modularity, it is poloidally faceted and presents a BZ organized in hexagonal bundles of radial fuel-breeder pins. These pins are a kind of bayonet heat exchanger, with an inner tube bringing cold He from the rear manifold to the BZ and a concentric annular channel consisting in the outer cladding bringing the heated He back to the manifold.

Fig. 2 shows a toroidal–radial and a toroidal–poloidal section of a slice of the outboard blanket in which the main components can be appreciated.

The Ceramic Breeder (CB), consisting in a mixture of Li_4SiO_4 and Li_2TiO_3 in a pebble bed form with an enrichment in ^{6}Li at 60%, is

Table 1
Neutronic reactions considered.

Number	Reaction	Threshold [MeV]	Q-Value [Mev]
1	$^{52}Cr(n,p)^{52}V$	$3.256{\cdot}10^{0}$	$-3.256{\cdot}10^{0}$
2	$^{52}Cr(n,2n)^{51}Cr$	$1.227{\cdot}10^{1}$	$-1.227{\cdot}10^{1}$
3	$^{55}Mn(n,2n)^{54}Mn$	$1.041{\cdot}10^{1}$	$-1.041{\cdot}10^{1}$
4	$^{54}Fe(n,p)^{54}Mn$	$3.397{\cdot}10^{-1}$	$-3.397{\cdot}10^{-1}$
5	$^{54}Fe(n,\alpha)^{51}Cr$	$6.759{\cdot}10^{-1}$	$-6.759{\cdot}10^{-1}$
6	$^{54}Fe(n,np)^{53}Mn$	$9.019{\cdot}10^{0}$	$-9.019{\cdot}10^{0}$
7	$^{56}Fe(n,p)^{56}Mn$	$4.100{\cdot}10^{0}$	$-4.100{\cdot}10^{0}$
8	$^{56}Fe(n,2n)^{55}Fe$	$1.140{\cdot}10^{1}$	$-1.140{\cdot}10^{1}$
9	$^{58}Ni(n,\alpha)^{55}Fe$	$0.000{\cdot}10^{0}$	$2.901{\cdot}10^{0}$
10	$^{58}Ni(n,p)^{58}Co$	$3.999{\cdot}10^{-1}$	$-3.999{\cdot}10^{-1}$
11	$^{58}Ni(n,2n)^{57}Ni$	$1.241{\cdot}10^{1}$	$-1.241{\cdot}10^{1}$
12	$^{58}Ni(n,np)^{57}Co$	$9.236{\cdot}10^{0}$	$-9.236{\cdot}10^{0}$
13	$^{60}Ni(n,p)^{60}Co$	$2.200{\cdot}10^{0}$	$-2.200{\cdot}10^{0}$

Table 2
Half-lives of the considered radioactive isotopes.

Recoil Nucleus	$T_{1/2}$
^{52}V	3.743 min
^{51}Cr	27.7025 d
^{54}Mn	312.081 d
^{53}Mn	$3.7{\cdot}10^{6}$ y
^{56}Mn	2.5789 h
^{55}Fe	2.737 y
^{57}Co	271.74 d
^{58}Co	70.86 d
^{60}Co	5.2714 y
^{57}Ni	35.60 h

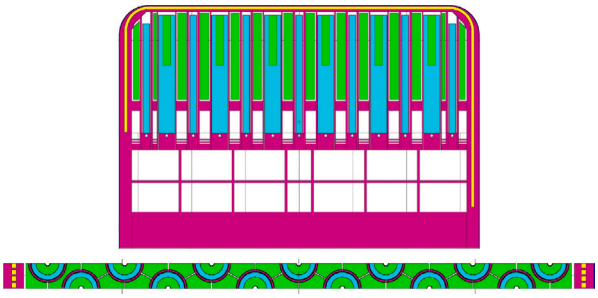

Fig. 3. MCNP model of the blanket equatorial outboard slice. Toroidal–radial section (up) and toroidal–poloidal section (down).

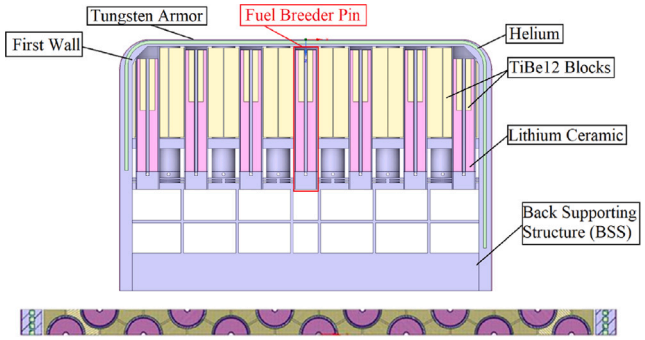

Fig. 2. Toroidal–radial and toroidal–poloidal sections of the equatorial slice of the outboard blanket.

positioned in between the pins' inner and outer cladding while the neutron multiplier material, that is $Be_{12}Ti$ in form of blocks, is located in the space among pressure tubes. He is employed both as coolant at 8 MPa, with T_{in} = 300 °C and T_{out} = 520 °C and purge gas flowing in the multiplier before and in the breeder then. As far as the structural material is concerned, EUROFER97 (Lindau et al., 2005) has been envisaged.

3.2. MCNP model

Neutronic analysis have been implemented adopting a MCNP model of a toroidal–radial slice of the Tokamak equatorial zone of the outboard blanket. The results have been roughly extended to the rest of the reactor in order to obtain a preliminary conservative assessment of the radioisotope inventories in the coolant, since the main purpose of this pilot work is to study the underlying physics of the phenomenon investigated and to develop a procedure to better address it, rather than to obtain precise quantitative results.

An initial CAD version of the outboard blanket slice (Fig. 2) has been slightly modified to match the adequate model definition for the neutronic analyses by SpaceClaim software (ANSYS Inc., 2021) and then converted in the constructive solid geometry representation adopted by MCNP by means of SuperMC code (Wu et al., 2015) (Fig. 3).

As far as materials are concerned, EUROfusion (EUROfusion, 2014) recommendations and database (Fischer and Qiu, 2020) have been adopted. In order to simulate the DEMO irradiation conditions, a plasma- facing surface source has been set up for the slice model properly biased in cosines and energies (Spagnuolo et al., 2019; Chiovaro et al., 2020). More precisely, the cosine and energy probability distributions of the neutron source have been evaluated using the results of an ad-hoc neutronic analysis performed by adopting the global MCNP model of DEMO equipped with the HCPB blanket (Zhou, 2021), in which neutrons crossing the plasma-facing surface in the equatorial zone of the outboard blanket, corresponding to the source surface of the slice model, have been tallied binning them in cosine and energy groups. In particular, the cosine distribution has been ranged in 10 subdivisions while the neutron energy has been divided in the 175 groups of the Vitamin J grid (Forrest et al., 2007). It is noteworthy to note that such a procedure allows to take into account not only the fusion reaction neutrons but also the albedo neutrons scattered elsewhere in the reactor. As for the boundary conditions are concerned, reflective ones were imposed in the poloidal and toroidal surfaces bounding the model to simulate the continuity of the geometry in these directions.

3.3. Results

The quantities of interest were calculated using the track length estimator tally (F4) in various ways, using the tally multiplier (FM) and

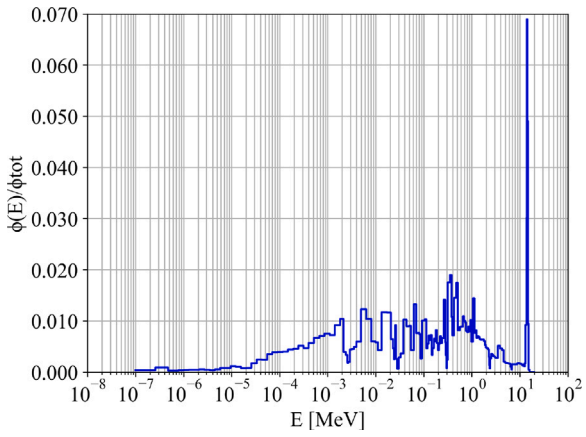

Fig. 4. Normalized flux in the FW.

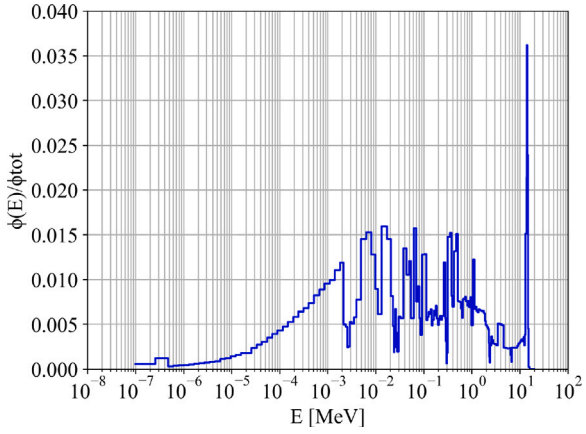

Fig. 5. Normalized flux in the BZ pins.

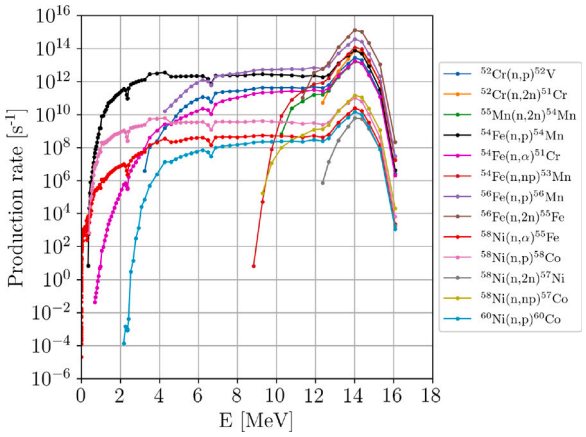

Fig. 6. Recoil nuclei production rate energy profiles in the FW.

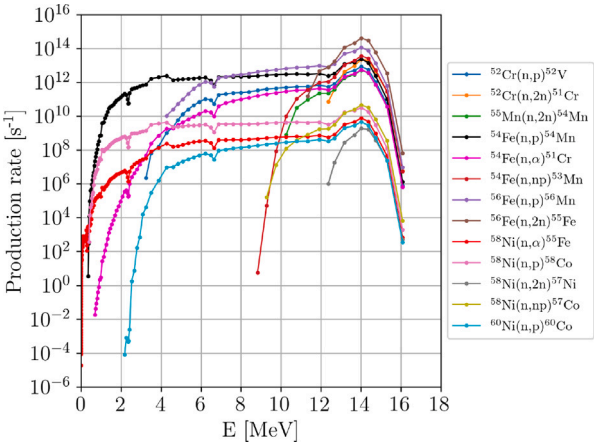

Fig. 7. Recoil nuclei production rate energy profiles in the BZ pins.

energy multiplier (EM) cards. Results related to extensive quantities were normalized to the plasma flat-top phase power of 1998 MW (Moro et al., 2021) corresponding to a neutron yield of $7.095 \cdot 10^{20}$ neutrons per second and taking into account the actual fraction of them which crosses the plasma-facing surface of the outboard slice considered. The results are affected by a statistical error of less than 0.1% as analyses have been performed using a very large number of histories (10^{11}) on the CRESCO cluster (Iannone et al., 2019). At this point it is helpful to recall that the DEMO duty cycle is characterized by a sequence of pulses, each consisting of a 100 s ramp-up transient, a 7200 s flat-top phase, a 100 s ramp-down transient and a 600 s dwell phase (Moscato et al., 2022).

Figs. 4 and 5 show the profile of flux (normalized to total flux) versus energy in the FW and BZ pins structural material.

It can be seen that the neutron spectrum is quite hard, especially, of course, in the FW that is the plasma face component. In both plots it can be noted that the main flux component is centered around 14 MeV as expected.

Figs. 6 and 7 show the production rates of the isotopes, that is the daughter nuclei of the considered reactions, in the FW and BZ pins respectively.

It is easy to observe that the energy profile of these quantities follows the flux profile quite closely. It is interesting to note that the production of ^{55}Fe from ^{58}Ni also peaks around 14 MeV, despite the fact that this (n, α) reaction is exoenergetic. This is due both to the aforementioned flux behavior and to the fact that this reaction has a broad and pronounced resonance peak around 10–11 MeV.

Table 3
Total recoil nuclei production rate [s^{-1}].

Reaction	FW	BZ pins
^{52}Cr(n,p)^{52}V	$7.292 \cdot 10^{13}$	$3.007 \cdot 10^{13}$
^{52}Cr(n,2n)^{51}Cr	$1.861 \cdot 10^{14}$	$6.071 \cdot 10^{13}$
^{55}Mn(n,2n)^{54}Mn	$4.193 \cdot 10^{13}$	$1.523 \cdot 10^{13}$
^{54}Fe(n,p)^{54}Mn	$2.566 \cdot 10^{14}$	$1.299 \cdot 10^{14}$
^{54}Fe(n, α)^{51}Cr	$4.636 \cdot 10^{13}$	$1.863 \cdot 10^{13}$
^{54}Fe(n,np)^{53}Mn	$2.896 \cdot 10^{14}$	$1.021 \cdot 10^{14}$
^{56}Fe(n,p)^{56}Mn	$9.810 \cdot 10^{14}$	$4.061 \cdot 10^{14}$
^{56}Fe(n,2n)^{55}Fe	$3.280 \cdot 10^{15}$	$1.133 \cdot 10^{15}$
^{58}Ni(n, α)^{55}Fe	$7.052 \cdot 10^{10}$	$3.161 \cdot 10^{10}$
^{58}Ni(n,p)^{58}Co	$3.653 \cdot 10^{11}$	$1.908 \cdot 10^{11}$
^{58}Ni(n,2n)^{57}Ni	$1.560 \cdot 10^{10}$	$5.010 \cdot 10^{9}$
^{58}Ni(n,np)^{57}Co	$3.714 \cdot 10^{11}$	$1.339 \cdot 10^{11}$
^{60}Ni(n,p)^{60}Co	$3.887 \cdot 10^{10}$	$1.646 \cdot 10^{10}$

For the sake of completeness, integral results for such production rates are given in Table 3, for both FW and BZ pins.

Table 4 shows the average energies E_1, E_2 and E_3, defined above, calculated in both the FW and BZ pins. Analysis of this table clearly shows the considerable differences between the values of the different averages, which can be one to two orders of magnitude. Moreover, the fact that $E_1 > E_2 > E_3$ indicates that the small percentage of low energy neutrons is characterized by large mean free paths (X-5 Monte Carlo Team, 2003).

Table 4
Average neutron energies in the FW and BZ pins per reaction.

Reactions	Average energies [MeV]					
	E_1		E_2		E_3	
	FW	BZ	FW	BZ	FW	BZ
^{52}Cr(n,p)^{52}V	$1.372\cdot10^{1}$	$1.314\cdot10^{1}$				
^{52}Cr(n2n)^{51}Cr	$1.416\cdot10^{1}$	$1.407\cdot10^{1}$				
^{55}Mn(n,2n)^{54}Mn	$1.405\cdot10^{1}$	$1.386\cdot10^{1}$				
^{54}Fe(n,p)^{54}Mn	$1.210\cdot10^{1}$	$1.100\cdot10^{1}$				
^{54}Fe(n, α)^{51}Cr	$1.383\cdot10^{1}$	$1.335\cdot10^{1}$				
^{54}Fe(n,np)^{53}Mn	$1.407\cdot10^{1}$	$1.392\cdot10^{1}$	3.056	2.318	$6.833\cdot10^{-2}$	$4.298\cdot10^{-2}$
^{56}Fe(n,p)^{56}Mn	$1.375\cdot10^{1}$	$1.320\cdot10^{1}$				
^{56}Fe(n,2n)^{55}Fe	$1.409\cdot10^{1}$	$1.397\cdot10^{1}$				
^{58}Ni(n, α)^{55}Fe	$1.316\cdot10^{1}$	$1.225\cdot10^{1}$				
^{58}Ni(n,p)^{58}Co	$1.155\cdot10^{1}$	$1.043\cdot10^{1}$				
^{58}Ni(n,2n)^{57}Ni	$1.417\cdot10^{1}$	$1.410\cdot10^{1}$				
^{58}Ni(n,np)^{57}Co	$1.405\cdot10^{1}$	$1.387\cdot10^{1}$				
^{60}Ni(n,p)^{60}Co	$1.366\cdot10^{1}$	$1.306\cdot10^{1}$				

Table 5
Average R-values in the FW per reaction.

Reaction	R-values [μm]						
	R_1	R_2	R_3	R_4	R_5	R_6	R_7
^{52}Cr(n,p)^{52}V	$1.423\cdot10^{-2}$	$2.636\cdot10^{-3}$	$4.189\cdot10^{-5}$	$9.672\cdot10^{-3}$	$1.072\cdot10^{-4}$	$0.000\cdot10^{0}$	$5.870\cdot10^{-2}$
^{52}Cr(n2n)^{51}Cr	$1.702\cdot10^{-2}$	$2.791\cdot10^{-3}$	$4.377\cdot10^{-5}$	$1.027\cdot10^{-2}$	$0.000\cdot10^{0}$	$0.000\cdot10^{0}$	$1.537\cdot10^{-1}$
^{55}Mn(n,2n)^{54}Mn	$2.346\cdot10^{-2}$	$4.017\cdot10^{-3}$	$6.309\cdot10^{-5}$	$1.970\cdot10^{-2}$	$0.000\cdot10^{0}$	$0.000\cdot10^{0}$	$1.675\cdot10^{-1}$
^{54}Fe(n,p)^{54}Mn	$8.066\cdot10^{-2}$	$3.301\cdot10^{-3}$	$5.332\cdot10^{-5}$	$1.711\cdot10^{-2}$	$5.093\cdot10^{-4}$	$0.000\cdot10^{0}$	$6.418\cdot10^{-2}$
^{54}Fe(n, α)^{51}Cr	$2.779\cdot10^{-2}$	$5.109\cdot10^{-3}$	$8.177\cdot10^{-5}$	$2.615\cdot10^{-2}$	$5.295\cdot10^{-4}$	$0.000\cdot10^{0}$	$9.126\cdot10^{-2}$
^{54}Fe(n,np)^{53}Mn	$2.048\cdot10^{-2}$	$3.500\cdot10^{-3}$	$5.502\cdot10^{-5}$	$7.999\cdot10^{-2}$	$0.000\cdot10^{0}$	$0.000\cdot10^{0}$	$1.251\cdot10^{-1}$
^{56}Fe(n,p)^{56}Mn	$1.262\cdot10^{-2}$	$2.326\cdot10^{-3}$	$3.691\cdot10^{-5}$	$1.178\cdot10^{-2}$	$4.716\cdot10^{-5}$	$0.000\cdot10^{0}$	$5.318\cdot10^{-2}$
^{56}Fe(n,2n)^{55}Fe	$1.748\cdot10^{-2}$	$2.946\cdot10^{-3}$	$4.624\cdot10^{-5}$	$1.672\cdot10^{-2}$	$0.000\cdot10^{0}$	$0.000\cdot10^{0}$	$1.393\cdot10^{-1}$
^{58}Ni(n, α)^{55}Fe	$3.866\cdot10^{-2}$	$8.306\cdot10^{-3}$	$5.869\cdot10^{-4}$	$4.138\cdot10^{-2}$	$2.958\cdot10^{-3}$	$4.818\cdot10^{-4}$	$1.147\cdot10^{-1}$
^{58}Ni(n,p)^{58}Co	$1.366\cdot10^{-2}$	$3.303\cdot10^{-3}$	$5.333\cdot10^{-5}$	$1.783\cdot10^{-2}$	$5.061\cdot10^{-4}$	$0.000\cdot10^{0}$	$6.411\cdot10^{-2}$
^{58}Ni(n,2n)^{57}Ni	$1.300\cdot10^{-2}$	$2.123\cdot10^{-3}$	$3.330\cdot10^{-5}$	$1.171\cdot10^{-2}$	$0.000\cdot10^{0}$	$0.000\cdot10^{0}$	$1.161\cdot10^{-1}$
^{58}Ni(n,np)^{57}Co	$1.752\cdot10^{-2}$	$3.008\cdot10^{-3}$	$4.728\cdot10^{-5}$	$1.711\cdot10^{-2}$	$0.000\cdot10^{0}$	$0.000\cdot10^{0}$	$1.082\cdot10^{-1}$
^{60}Ni(n,p)^{60}Co	$1.391\cdot10^{-2}$	$2.608\cdot10^{-3}$	$4.161\cdot10^{-5}$	$1.417\cdot10^{-2}$	$2.030\cdot10^{-4}$	$0.000\cdot10^{0}$	$5.430\cdot10^{-2}$

Table 6
Average R-values in the BZ pins per reaction.

Reaction	R-values [μm]						
	R_1	R_2	R_3	R_4	R_5	R_6	R_7
^{52}Cr(n,p)^{52}V	$1.298\cdot10^{-2}$	$1.766\cdot10^{-3}$	$2.178\cdot10^{-5}$	$7.481\cdot10^{-3}$	$2.082\cdot10^{-5}$	$0.000\cdot10^{0}$	$5.870\cdot10^{-2}$
^{52}Cr(n2n)^{51}Cr	$1.653\cdot10^{-2}$	$4.787\cdot10^{-3}$	$2.048\cdot10^{-5}$	$6.335\cdot10^{-3}$	$0.000\cdot10^{0}$	$0.000\cdot10^{0}$	$1.537\cdot10^{-1}$
^{55}Mn(n,2n)^{54}Mn	$2.226\cdot10^{-2}$	$2.510\cdot10^{-3}$	$3.022\cdot10^{-5}$	$1.594\cdot10^{-2}$	$0.000\cdot10^{0}$	$0.000\cdot10^{0}$	$1.675\cdot10^{-1}$
^{54}Fe(n,p)^{54}Mn	$1.219\cdot10^{-2}$	$2.251\cdot10^{-3}$	$2.844\cdot10^{-5}$	$1.574\cdot10^{-2}$	$2.653\cdot10^{-4}$	$0.000\cdot10^{0}$	$6.418\cdot10^{-2}$
^{54}Fe(n, α)^{51}Cr	$2.580\cdot10^{-2}$	$3.448\cdot10^{-3}$	$4.297\cdot10^{-5}$	$2.356\cdot10^{-2}$	$2.409\cdot10^{-4}$	$0.000\cdot10^{0}$	$9.126\cdot10^{-2}$
^{54}Fe(n,np)^{53}Mn	$1.969\cdot10^{-2}$	$2.217\cdot10^{-3}$	$2.675\cdot10^{-5}$	$4.708\cdot10^{-3}$	$0.000\cdot10^{0}$	$0.000\cdot10^{0}$	$1.251\cdot10^{-1}$
^{56}Fe(n,p)^{56}Mn	$1.155\cdot10^{-2}$	$1.552\cdot10^{-3}$	$1.908\cdot10^{-5}$	$1.041\cdot10^{-2}$	$2.106\cdot10^{-6}$	$0.000\cdot10^{0}$	$5.318\cdot10^{-2}$
^{56}Fe(n,2n)^{55}Fe	$1.681\cdot10^{-2}$	$1.821\cdot10^{-3}$	$2.189\cdot10^{-5}$	$1.621\cdot10^{-2}$	$0.000\cdot10^{0}$	$0.000\cdot10^{0}$	$1.393\cdot10^{-1}$
^{58}Ni(n, α)^{55}Fe	$3.429\cdot10^{-2}$	$5.925\cdot10^{-3}$	$5.265\cdot10^{-4}$	$4.024\cdot10^{-2}$	$2.114\cdot10^{-3}$	$4.706\cdot10^{-4}$	$1.147\cdot10^{-1}$
^{58}Ni(n,p)^{58}Co	$1.128\cdot10^{-2}$	$2.253\cdot10^{-3}$	$2.844\cdot10^{-5}$	$1.738\cdot10^{-2}$	$2.617\cdot10^{-4}$	$0.000\cdot10^{0}$	$6.411\cdot10^{-2}$
^{58}Ni(n,2n)^{57}Ni	$1.269\cdot10^{-2}$	$1.297\cdot10^{-3}$	$1.557\cdot10^{-5}$	$1.114\cdot10^{-2}$	$0.000\cdot10^{0}$	$0.000\cdot10^{0}$	$1.161\cdot10^{-1}$
^{58}Ni(n,np)^{57}Co	$1.673\cdot10^{-2}$	$1.902\cdot10^{-3}$	$2.295\cdot10^{-5}$	$1.676\cdot10^{-2}$	$0.000\cdot10^{0}$	$0.000\cdot10^{0}$	$1.082\cdot10^{-1}$
^{60}Ni(n,p)^{60}Co	$1.268\cdot10^{-2}$	$1.760\cdot10^{-3}$	$2.184\cdot10^{-5}$	$1.371\cdot10^{-2}$	$7.120\cdot10^{-5}$	$0.000\cdot10^{0}$	$5.430\cdot10^{-2}$

Tables 5 and 6 show the average R-values in the FW and in BZ pins.

It holds always that $R_1 > R_2 > R_3$, this confirms that sputtering is a phenomenon essentially related to faster neutrons and shows that it is precisely the higher energy component of the flux that leads to both a higher rate of radioisotope production (Figs. 6 and 7) and a greater range of radioisotope progression in the structural material, as expected.

The 0 values of R_5 and R_6 refer to those reactions for which the threshold energy is greater than E_2 and E_3 respectively. It is very interesting to note that among the reactions considered for ^{54}Fe(n,p)^{54}Mn it turns out that R_1 is greater than R_7 in the FW. This highlights the importance of the right tail of the Gaussian distribution of fusion neutron energy and shows that considering 14.1 MeV for the incident neutron energy when calculating R_7 cannot generally be considered a conservative approach. Obviously, this observation is even more valid for the R-values calculated with E_D corresponding to a 14.1 MeV neutron energy, as these values are lower than R_1 for many reactions.

It is also observed that the R-values obtained with a given pdf are very different from the R-values obtained with the mean energies obtained with the same pdf (E_i, $i = 1, 2, 3$). This implies that function

Table 7
ACM flow rates.

Recoil Nucleus	R_s	Q''' [$m^{-3}s^{-1}$] Slice		q'' [$m^{-2}s^{-1}$] Slice		G [gs^{-1}] Whole blanket		
		FW	BZ	FW	BZ	FW	BZ	Total
$^{52}Cr(n,p)^{52}V$	R_1	$7.653\cdot10^{-2}$	$5.027\cdot10^{-2}$	$3.816\cdot10^{7}$	$2.287\cdot10^{7}$	$2.552\cdot10^{-13}$	$5.436\cdot10^{-13}$	$7.988\cdot10^{-13}$
	R_7			$1.574\cdot10^{8}$	$1.034\cdot10^{8}$	$1.053\cdot10^{-12}$	$2.458\cdot10^{-12}$	$3.511\cdot10^{-12}$
$^{52}Cr(n,2n)^{51}Cr$	R_1	$1.954\cdot10^{-1}$	$1.015\cdot10^{-1}$	$1.165\cdot10^{8}$	$5.880\cdot10^{7}$	$7.641\cdot10^{-13}$	$1.371\cdot10^{-12}$	$2.135\cdot10^{-12}$
	R_7			$1.052\cdot10^{9}$	$5.465\cdot10^{8}$	$6.900\cdot10^{-12}$	$1.274\cdot10^{-11}$	$1.964\cdot10^{-11}$
$^{55}Mn(n,2n)^{54}Mn$	R_1	$4.401\cdot10^{-2}$	$2.547\cdot10^{-2}$	$3.618\cdot10^{7}$	$1.987\cdot10^{7}$	$2.513\cdot10^{-13}$	$4.905\cdot10^{-13}$	$7.418\cdot10^{-13}$
	R_7			$2.583\cdot10^{8}$	$1.495\cdot10^{8}$	$1.794\cdot10^{-12}$	$3.690\cdot10^{-12}$	$5.484\cdot10^{-12}$
$^{54}Fe(n,p)^{54}Mn$	R_1	$2.694\cdot10^{-1}$	$2.172\cdot10^{-1}$	$7.614\cdot10^{8}$	$9.278\cdot10^{7}$	$5.288\cdot10^{-12}$	$2.290\cdot10^{-12}$	$7.579\cdot10^{-12}$
	R_7			$6.058\cdot10^{8}$	$4.885\cdot10^{8}$	$4.208\cdot10^{-12}$	$1.206\cdot10^{-11}$	$1.627\cdot10^{-11}$
$^{54}Fe(n,\alpha)^{51}Cr$	R_1	$4.866\cdot10^{-2}$	$3.115\cdot10^{-2}$	$4.738\cdot10^{7}$	$2.817\cdot10^{7}$	$3.108\cdot10^{-13}$	$6.567\cdot10^{-13}$	$9.675\cdot10^{-13}$
	R_7			$1.556\cdot10^{8}$	$9.962\cdot10^{7}$	$1.021\cdot10^{-12}$	$2.323\cdot10^{-12}$	$3.343\cdot10^{-12}$
$^{54}Fe(n,np)^{53}Mn$	R_1	$3.040\cdot10^{-1}$	$1.708\cdot10^{-1}$	$2.182\cdot10^{8}$	$1.178\cdot10^{8}$	$1.487\cdot10^{-12}$	$2.855\cdot10^{-12}$	$4.342\cdot10^{-12}$
	R_7			$1.333\cdot10^{9}$	$7.485\cdot10^{8}$	$9.083\cdot10^{-12}$	$1.814\cdot10^{-11}$	$2.722\cdot10^{-11}$
$^{56}Fe(n,p)^{56}Mn$	R_1	$1.030\cdot10^{0}$	$6.789\cdot10^{-1}$	$4.555\cdot10^{8}$	$2.749\cdot10^{8}$	$3.281\cdot10^{-12}$	$7.037\cdot10^{-12}$	$1.032\cdot10^{-11}$
	R_7			$1.919\cdot10^{9}$	$1.265\cdot10^{9}$	$1.382\cdot10^{-11}$	$3.239\cdot10^{-11}$	$4.621\cdot10^{-11}$
$^{56}Fe(n,2n)^{55}Fe$	R_1	$3.443\cdot10^{0}$	$1.894\cdot10^{0}$	$2.109\cdot10^{9}$	$1.116\cdot10^{9}$	$1.492\cdot10^{-11}$	$2.755\cdot10^{-11}$	$4.247\cdot10^{-11}$
	R_7			$1.681\cdot10^{10}$	$9.248\cdot10^{9}$	$1.535\cdot10^{-12}$	$2.806\cdot10^{-11}$	$2.960\cdot10^{-11}$
$^{58}Ni(n,\alpha)^{55}Fe$	R_1	$7.402\cdot10^{-5}$	$5.285\cdot10^{-5}$	$1.003\cdot10^{5}$	$6.350\cdot10^{4}$	$7.093\cdot10^{-16}$	$1.596\cdot10^{-15}$	$2.306\cdot10^{-15}$
	R_7			$2.976\cdot10^{5}$	$2.125\cdot10^{5}$	$2.105\cdot10^{-15}$	$5.342\cdot10^{-15}$	$7.448\cdot10^{-15}$
$^{58}Ni(n,p)^{58}Co$	R_1	$3.835\cdot10^{-4}$	$3.190\cdot10^{-4}$	$1.836\cdot10^{5}$	$1.261\cdot10^{5}$	$1.369\cdot10^{-15}$	$3.342\cdot10^{-15}$	$4.711\cdot10^{-15}$
	R_7			$8.616\cdot10^{5}$	$7.167\cdot10^{5}$	$6.427\cdot10^{-15}$	$1.900\cdot10^{-14}$	$2.543\cdot10^{-14}$
$^{58}Ni(n,2n)^{57}Ni$	R_1	$1.638\cdot10^{-5}$	$8.374\cdot10^{-6}$	$7.462\cdot10^{3}$	$3.723\cdot10^{3}$	$5.470\cdot10^{-17}$	$9.700\cdot10^{-17}$	$1.517\cdot10^{-16}$
	R_7			$6.661\cdot10^{4}$	$3.406\cdot10^{4}$	$4.883\cdot10^{-16}$	$8.875\cdot10^{-16}$	$1.376\cdot10^{-15}$
$^{58}Ni(n,np)^{57}Co$	R_1	$3.898\cdot10^{-4}$	$2.238E\cdot10^{-4}$	$2.394\cdot10^{5}$	$1.312\cdot10^{5}$	$1.755\cdot10^{-15}$	$3.419\cdot10^{-15}$	$5.174\cdot10^{-15}$
	R_7			$1.478\cdot10^{6}$	$8.486\cdot10^{5}$	$1.084\cdot10^{-14}$	$2.211\cdot10^{-14}$	$3.295\cdot10^{-14}$
$^{60}Ni(n,p)^{60}Co$	R_1	$4.080\cdot10^{-5}$	$2.751\cdot10^{-5}$	$1.989\cdot10^{4}$	$1.223\cdot10^{4}$	$1.535\cdot10^{-16}$	$3.354\cdot10^{-16}$	$4.888\cdot10^{-16}$
	R_7			$7.764\cdot10^{4}$	$5.234\cdot10^{4}$	$5.992\cdot10^{-16}$	$1.436\cdot10^{-15}$	$2.035\cdot10^{-15}$

Table 8
Comparison between radio-isotopes mass flow rates [gs^{-1}] towards the coolant in the WCLL and HCPB blankets.

Recoil Nucleus	WCLL	HCPB (via R_7 values)	Ratio
^{52}V	$4.007\cdot10^{-13}$	$3.511\cdot10^{-12}$	$1.141\cdot10^{-1}$
^{51}Cr	$1.881\cdot10^{-9}$	$2.299\cdot10^{-11}$	$8.183\cdot10^{1}$
^{54}Mn	$1.100\cdot10^{-8}$	$2.175\cdot10^{-11}$	$5.058\cdot10^{2}$
^{53}Mn	$3.692\cdot10^{-8}$	$2.722\cdot10^{-11}$	$1.356\cdot10^{3}$
^{56}Mn	$2.447\cdot10^{-11}$	$4.621\cdot10^{-11}$	$5.296\cdot10^{-1}$
^{55}Fe	$3.447\cdot10^{-7}$	$2.960\cdot10^{-11}$	$1.164\cdot10^{4}$
^{58}Co	$1.915\cdot10^{-10}$	$2.543\cdot10^{-14}$	$7.529\cdot10^{3}$
^{57}Ni	$4.796\cdot10^{-12}$	$1.376\cdot10^{-15}$	$3.486\cdot10^{3}$
^{57}Co	$2.750\cdot10^{-10}$	$3.295\cdot10^{-14}$	$8.346\cdot10^{3}$
^{60}Co	$1.301\cdot10^{-9}$	$2.035\cdot10^{-15}$	$6.394\cdot10^{5}$

$R(E)$ has a strong non-linear behavior, at least around the mean value of its variable.

Moreover, it is noteworthy to note that the calculated R_1 and R_7 values are rather close to the experimental values shown in Lessor et al. (1977).

The results obtained have been roughly extrapolated to the entire HCPB blanket of DEMO, assuming that it is seamless (no ports, antenna openings and so on) and subjected to a uniform neutron load equal to that of the slice considered, which is one of the highest (Chiovaro et al., 2020). Naturally, this leads to very conservative values, which can be considered as a kind of unattainable maximum. Table 7 reports the volumetric density of the daughter isotope production rates (Q'''), its flux rates (q'') and mass flow rates (G) towards the coolant both in the FW and the BZ pins, taking into account as R-values R_1 and R_7, considered as the most reliable and the limiting values respectively.

Using the nuclear data required for the work presented in Terranova et al. (2024), a comparison (Table 8) is made between the mass flow rates of the radioisotopes in question towards the cooling water of the DEMO Water Cooled Lithium Lead (WCLL) (Del Nevo et al., 2019) blanket (Activated Corrosion Products (ACPs)) and the helium of the HCPB blanket (sputtered ACMs). It is useful to note that WCLL and HCPB are, to date, the two blanket concepts from which the EU will have to choose the one to be integrated in the final European DEMO reactor design (Boccaccini et al., 2022; Spagnuolo et al., 2021). In this respect, it is noted that such a comparison is necessary, but at the same time it is emphasized that it should be assessed with caution. Indeed, the way in which the radioisotopes are released into the coolant is profoundly different in the two blanket concepts, even involving non-trivial chemical balances in the case of WCLL. So, a number of variables come into play, such as reactor operating scenarios, maintenance criteria and water chemistry management, which make the comparison we are dealing with very difficult.

The mass flow rates for the WCLL have been calculated following the approach proposed by Kennedy (1976), i.e. by solving a set of seven ordinary differential equations for each considered radio-isotope, to preliminary provide the expected order of magnitude of the ACPs releases into cooling water of the WCLL. These equations describe the mass balances of each radio-isotope and their parent species in the coolant, in the in-vessel components, and in both the in- and ex-vessel oxide layers.

In the WCLL the radio-isotopes mass flow rates are provided for the entire blanket, net of redeposition from the coolant, and time-averaged in 5 years of full-power operation that is the envisaged life of DEMO blankets.

So, Table 8 shows that the aptitude to coolant contamination is less of an issue for the HCPB blanket than for the WCLL for most of the species, bearing in mind also that the data relating to the WCLL are not as limiting as those for the HCPB, given the above assumptions

for extrapolating the results from the slice to the whole reactor and the selection of production rates obtained by the use of R_7. The only exceptions are ^{52}V and ^{56}Mn, which in the WCLL case, due to their short half-lives, are produced inside the oxide layers and decay before being released into the coolant. In any case, it is important to note that the design development of both concepts is still too immature to make a valid quantitative assessment. Indeed, it is noted that the WCLL design would require a more accurate assessment of the concentration of isotopes dispersed in water by corrosion and a more detailed design of the HCPB blanket lay-out should be considered.

4. Conclusions

This paper addresses the problem of contamination of the hydraulic circuits of gas-cooled nuclear reactors by radioisotopes formed as a result of nuclear reactions in the structural material. This phenomenon is dominated by the sputtering of the daughter nuclei towards the coolant, and in this regard an original theoretical model has been developed which makes it possible to obtain quantitative evaluations of the flow of radioactive nuclei reaching the coolant. Therefore, an original method has been developed to provide a calculation procedure that is both scientifically robust and quite flexible from an operational point of view. It consists of the determination of a suitable average range of recoil nuclei by Monte Carlo analysis and a simple evaluation of the given radioisotope flow in the cooling gas.

A numerical implementation of this model was therefore carried out using the HCPB blanket of the DEMO fusion reactor as a reference and adopting a sub-modeling approach.

The nuclear response of this blanket was evaluated in terms of the neutron spectrum and the production rates of the radioisotopes of interest, in order to frame the underlying physics of the studied phenomenology, finding it is strongly influenced by the faster components of the neutron flux.

With regard to the evaluation of the radioisotope flow towards the coolant, the characteristic quantity of the developed model, that is the range of the recoil nuclei, was studied. This study provided the necessary elements to deduce that the average, weighted over the relative production rate, of this range is the quantity to be considered as most reliable for dealing with the problem addressed. Finally, a rough preliminary assessment of the inventory of radioisotopes from the structural material reaching the coolant in the DEMO HCPB blanket was made and then compared with that calculated for the ACPs in the WCLL blanket concept in the same DEMO baseline. This comparison showed that the problem of coolant contamination is much more severe in the WCLL than in the HCPB concept.

CRediT authorship contribution statement

P. Chiovaro: Conceptualization, Methodology, Investigation, Writing – original draft. **L. Girard:** Conceptualization, Methodology, Investigation, Writing – original draft. **A. Quartararo:** Conceptualization, Methodology, Investigation, Writing – original draft. **S. Basile:** Conceptualization, Methodology, Investigation, Writing – original draft. **G. Bongiovì:** Conceptualization, Methodology, Investigation, Writing – original draft. **P.A. Di Maio:** Conceptualization, Methodology, Investigation, Writing – original draft. **I. Moscato:** Conceptualization, Methodology, Investigation, Writing – original draft. **E. Vallone:** Conceptualization, Methodology, Investigation, Writing – original draft. **G. Zhou:** Conceptualization, Methodology, Investigation, Writing – original draft.

Declaration of competing interest

The authors declare that they have no known competing financial interests or personal relationships that could have appeared to influence the work reported in this paper.

Acknowledgments

This work has been carried out within the framework of the EUROfusion Consortium, funded by the European Union via the Euratom Research and Training Programme (Grant Agreement No 101052200 — EUROfusion). Views and opinions expressed are however those of the author(s) only and do not necessarily reflect those of the European Union or the European Commission. Neither the European Union nor the European Commission can be held responsible for them.

The computing resources and the related technical support used for this work have been provided by CRESCO/ENEAGRID High Performance Computing infrastructure and its staff (Iannone et al., 2019). CRESCO/ENEAGRID High Performance Computing infrastructure is funded by ENEA, the Italian National Agency for New Technologies, Energy and Sustainable Economic Development and by Italian and European research programmes, see http://www.cresco.enea.it/english for information.

Appendix A

To derive Eq. (7) it is convenient to start from rewriting Eq. (6) in a proper way:

$$R\left(E_{\mathrm{D}}\right)=\frac{1}{f_1}\int_{E_{\mathrm{D}}}^{0}\frac{E}{\ln\left(f_2E\right)}\mathrm{d}E \tag{A.1}$$

if $\epsilon=f_2E$ then

$$R\left(E_{\mathrm{D}}\right)=\frac{1}{f_1f_2^2}\int_{f_2E_{\mathrm{D}}}^{0}\frac{\epsilon}{\ln\left(\epsilon\right)}\mathrm{d}\epsilon \tag{A.2}$$

Using the variable change $y=-\ln\left(\epsilon\right)$, so that

$$R\left(E_{\mathrm{D}}\right)=\frac{1}{f_1f_2^2}\int_{-\ln(f_2E_{\mathrm{D}})}^{+\infty}\frac{e^{-2y}}{y}\mathrm{d}y \tag{A.3}$$

And, putting $z=2y$:

$$R\left(E_{\mathrm{D}}\right)=\frac{1}{f_1f_2^2}\int_{-2\ln(f_2E_{\mathrm{D}})}^{+\infty}\frac{e^{-z}}{z}\mathrm{d}z \tag{A.4}$$

which gives Eq. (7) by definition.

Appendix B

Let us consider the neutron reaction $X(n,b)D$. As usual it is advantageous to derive the energy of the recoil nucleus in the laboratory frame, K_{D}, starting from the center of mass frame (Lamarsh, 1972; Krane, 1988):

$$K_{\mathrm{D}}=\frac{1}{2}m_{\mathrm{D}}\left(V_{\mathrm{D_{cm}}}^2+V_{\mathrm{cm}}^2+2V_{\mathrm{D_{cm}}}V_{\mathrm{cm}}\cos(\vartheta_{\mathrm{cm}})\right) \tag{B.1}$$

Where the subscript "cm" points at quantities related to the center of mass frame. For V_{cm} the following formula holds (Bethe and Heitler, 1934):

$$V_{\mathrm{cm}}=\frac{m_n}{m_n+m_X}\sqrt{\frac{2E_n}{m_n}} \tag{B.2}$$

m_n and m_X being the masses of the incident neutron and the target nucleus, respectively.

It is assumed that the emission of the compound nucleus is isotropic in the center of mass frame (i.e. the angular distribution of the reaction products is uniform), so it holds that:

$$E_{\mathrm{D}}=\frac{1}{\pi}\int_0^{\pi}K_{\mathrm{D}}\left(\vartheta_{\mathrm{cm}}\right)\mathrm{d}\vartheta_{\mathrm{cm}}=\frac{1}{2}m_{\mathrm{D}}\left(V_{\mathrm{D_{cm}}}^2+V_{\mathrm{cm}}^2\right)=T_{\mathrm{D_{cm}}}+\frac{1}{2}m_{\mathrm{D}}V_{\mathrm{cm}}^2 \tag{B.3}$$

where $T_{\mathrm{D_{cm}}}$ is the energy of the daughter nucleus in the center of mass frame, while its maximum energy $E_{\mathrm{D_{MAX}}}$ is:

$$E_{\mathrm{D_{MAX}}}=\frac{1}{2}m_{\mathrm{D}}\left(V_{\mathrm{D_{cm}}}^2+V_{\mathrm{cm}}^2+2V_{\mathrm{D_{cm}}}V_{\mathrm{cm}}\right) \tag{B.4}$$

The following formula can be used for $T_{D_{cm}}$:

$$T_{D_{cm}} = \left(\frac{m_X}{m_n + m_X} E_n + Q \right) \frac{m_b}{m_b + m_D} \tag{B.5}$$

Using Eqs. (B.2) and (B.5), Eq. (B.3) after some algebra can be rewritten in the following way (Krane, 1988):

$$E_D = AE_n + C \tag{B.6}$$

where

$$A = \left[\frac{m_X m_b}{(m_n + m_X)(m_b + m_D)} + \frac{m_n m_D}{(m_X + m_n)^2} \right] \tag{B.7}$$

and

$$C = \frac{m_b}{m_b + m_D} Q \tag{B.8}$$

are the coefficients present in Eqs. (8) and (9).

Data availability

Data will be made available on request.

References

Abramowitz, M., Stegun, I., 1965. Handbook of mathematical functions. Applied mathematical series, Dover.

ANSYS Inc., 2021. Discovery SpaceClaim. ANSYS, Canonsburg, PA, USA, 2021 Release: 2021 R1.

Bang-jiao, Y., et al., 1999. Reduced sputtering yields induced by fast neutrons. Chin. Phys. Lett. 16 (11), 844. http://dx.doi.org/10.1088/0256-307X/16/11/024.

Behrisch, R., 1983. In: Behrish, R. (Ed.), Sputtering by Particle Bombardment II: Sputtering of Alloys and Compounds, Electron and Neutron Sputtering, Surface Topography. Springer Berlin Heidelberg, Berlin, Heidelberg, pp. 179–229. http://dx.doi.org/10.1007/3-540-12593-0_5.

Bethe, H., Heitler, W., 1934. On the stopping of fast particles and on the creation of positive electrons. Proc. Roy. Soc. Lond. A 146, 83–112. http://dx.doi.org/10.1098/rspa.1934.0140.

Bickford, W., 1980. Transport and Deposition of Activation Products in a Helium Cooled Fusion Power Plant. Tech. rep, Battelle Pacific Northwest Labs..

Blin-Stoyle, R.J., 1991. Nuclear and particle physics. In: Physics and its applications, Chapman and Hall.

Boccaccini, L., et al., 2022. Status of maturation of critical technologies and systems design: Breeding blanket. Fusion Eng. Des. 179, 113116. http://dx.doi.org/10.1016/j.fusengdes.2022.113116.

Brassert, W.L., Gardiner, G.K., Morse, F.H., 1959. Recoil Activity from Stainless-steel Cladding: A Major Contribution to Coolant-stream Radioactivity in GCR-2. Tech. rep, Massachusetts Inst. of Tech., Oak Ridge, Tenn. Engineering Practice School.

Chiovaro, P., et al., 2020. Investigation of the DEMO WCLL breeding blanket cooling water activation. Fusion Eng. Des. 157, 111697. http://dx.doi.org/10.1016/j.fusengdes.2020.111697.

Del Nevo, A., et al., 2019. Recent progress in developing a feasible and integrated conceptual design of the WCLL BB in eurofusion project. Fusion Eng. Des. 146, 1805–1809. http://dx.doi.org/10.1016/j.fusengdes.2019.03.040, SI:SOFT-30.

EUROfusion, 2014. EUROfusion webpage, post=URL ,. https://euro-fusion.org/eurofusion/.

Evans, R., 1955. The atomic nucleus. In: International series in pure and applied physics, vol. 582, McGraw-Hill.

Federici, G., Baylard, C., Beaumont, A., Holden, J., 2021. The plan forward for EU DEMO. Fusion Eng. Des. 173, 112960. http://dx.doi.org/10.1016/j.fusengdes.2021.112960.

Federici, G., et al., 2019. Overview of the DEMO staged design approach in europe. Nucl. Fusion 59, 066013. http://dx.doi.org/10.1088/1741-4326/ab1178.

Firestone, R., 1999. Table of Isotopes, eighth ed. Wiley, ISBN: 978-0-471-35633-2,

Fischer, U., Qiu, Y., 2020. Material compositions for PPPT neutronics and activation analyses. EUROfusion IDM Ref.: 2MM3A6 v1.1.

Forrest, R., Kopecky, J., Sublet, J.-C., 2007. The European activation file: EAF-2007 neutron-induced cross section library. UKAEA FUS 535.

Forty, C., Kardistas, P.J., 1994. Activation Product Transport and Deposition in the Helium Cooling Circuit of the SEAFP Reference Plant Model. Tech. rep., UKAEA Government Division, Fusion, Culham, Abingdon, Oxfordshire, OX143DB, UK.

Grimes, D.R., Warren, D.R., Partridge, M., 2017. An approximate analytical solution of the bethe equation for charged particles in the radiotherapeutic energy range. Sci. Rep. 7, 9781. http://dx.doi.org/10.1038/s41598-017-10554-0.

Harling, O., Thomas, M., Brodzinski, R., Rancitelli, L., 1976. Recent neutron sputtering results and the status of neutron sputtering. J. Nucl. Mater. 63, 422–428. http://dx.doi.org/10.1016/0022-3115(76)90359-7.

IAEA, 2012. Modelling of Transport of Radioactive Substances in the Primary Circuit of Water Cooled Reactors. In: TECDOC Series, (no. 1672), INTERNATIONAL ATOMIC ENERGY AGENCY, Vienna.

Iannone, F., et al., 2019. CRESCO ENEA HPC clusters: a working example of a multifabric gpfs spectrum scale layout. In: 2019 International Conference on High Performance Computing Simulation. HPCS, pp. 1051–1052.

Kaminsky, M., Das, S., 1976. 14.1-MeV neutron sputtering of polycrystalline and monocrystalline niobium with different surface microstructures. J. Nucl. Mater. 60, 111–116.

Karditsas, P.J., Forty, C., 1997. Modelling and simulation of activation product transport in helium cooling loops. Fusion Eng. Des. 36 (2), 203–217. http://dx.doi.org/10.1016/S0920-3796(96)00703-X, Invited Papers of the 19th Symposium on Fusion Technology.

Kennedy, A., 1976. PWR crud characterization and transport modeling. In: Proc. System Contamination Workshop, EPRI. p. 96.

Klein, A., Vogelsang, W., 1985. Radiation hazards due to activated corrosion and neutron sputtering products in fusion reactor coolant and tritium breeding fluids. Nuclear Eng. Design Fusion 2 (3), 355–363. http://dx.doi.org/10.1016/0167-899X(85)90023-0.

Krane, K., 1988. Introductory Nuclear Physics. Wiley.

Lamarsh, J., 1972. Introduction to nuclear reactor theory. In: Addison-Wesley series in nuclear engineering, Addison-Wesley.

Lessor, D.L., Thomas, M.T., Harling, O.K., 1977. Projected range calculations of radionuclide product ejection from metal surfaces by 14.8-MeV neutrons. J. Appl. Phys. 48 (10), 4337–4343. http://dx.doi.org/10.1063/1.323424.

Lindau, R., et al., 2005. Present development status of EUROFER and ODS-EUROFER for application in blanket concepts. Fusion Eng. Des. 75–79, 989–996. http://dx.doi.org/10.1016/j.fusengdes.2005.06.186.

Moro, F., et al., 2021. Nuclear performances of the water-cooled lithium lead DEMO reactor: Neutronic analysis on a fully heterogeneous model. Fusion Eng. Des. 168, 112514. http://dx.doi.org/10.1016/j.fusengdes.2021.112514.

Moscato, I., et al., 2022. Tokamak cooling systems and power conversion system options. Fusion Eng. Des. 178, 113093. http://dx.doi.org/10.1016/j.fusengdes.2022.113093.

National Research Council, 1996. Radiochemistry in nuclear power reactors. The National Academies Press, Washington, DC, http://dx.doi.org/10.17226/9263.

NEA, 2017. JEFF3.3 nuclear data library. https://www.oecd-nea.org/dbdata/jeff/jeff33/#neutron.

Neeb, K.-H., 1997. The Radiochemistry of Nuclear Power Plants with Light Water Reactors. De Gruyter, Berlin, New York, http://dx.doi.org/10.1515/9783110812015.

Salvat, F., 2022. Bethe stopping-power formula and its corrections. Phys. Rev. A 106, 032809. http://dx.doi.org/10.1103/PhysRevA.106.032809.

Sigmund, P., 1969. Theory of sputtering. I. Sputtering yield of amorphous and polycrystalline targets. Phys. Rev. 184, 383–416. http://dx.doi.org/10.1103/PhysRev.184.383.

Spagnuolo, G.A., Chiovaro, P., Di Maio, P.A., Favetti, R., 2019. A multi-physics integrated approach to breeding blanket modelling and design. Fusion Eng. Des. 143, 35–40. http://dx.doi.org/10.1016/j.fusengdes.2019.03.131.

Spagnuolo, G., et al., 2021. Integrated design of breeding blanket and ancillary systems related to the use of helium or water as a coolant and impact on the overall plant design. Fusion Eng. Des. 173, 112933. http://dx.doi.org/10.1016/j.fusengdes.2021.112933.

Terranova, N., Chiovaro, P., Dacquait, F., Moscato, I., Vallone, E., 2024. Activated corrosion product contamination assessments of DEMO WCLL breeding blanket primary heat transport system. Fusion Eng. Des. 199, 114132. http://dx.doi.org/10.1016/j.fusengdes.2023.114132.

Terranova, N., Di Pace, L., 2021. DEMO wcll primary heat transfer system loops activated corrosion products assessment. Fusion Eng. Des. 170, 112456. http://dx.doi.org/10.1016/j.fusengdes.2021.112456.

Wu, Y., et al., 2015. CAD-based Monte Carlo program for integrated simulation of nuclear system supermc. Ann. Nucl. Energy 82, 161–168. http://dx.doi.org/10.1016/j.anucene.2014.08.058.

X-5 Monte Carlo Team, 2003. MCNP – A General Monte Carlo N-Particle Transport Code, Version 5. LANL, Los Alamos, New Mexico, USA (April 2003).

Ye, B., Kasugai, Y., Ikeda, Y., 1997. Systematic study on sputtering yields by 14.9 MeV neutrons. Tech. rep., Japan Atomic Energy Research Inst..

Ye, B., et al., 2001. Radioactivity sputtered from cooling-pipe materials into coolant in the ITER cooling system. Fusion Sci. Technol. 40 (2), 133–138. http://dx.doi.org/10.13182/FST01-A187.

Zhou, G., 2021. Deliverable BB-s.02.01-t001-d009, HCPB design and analysis – report 2022. EUROfusion IDM Ref.: 2R6HXT v1.0.

Zhou, G., Hernández, F.A., Pereslavtsev, P., Kiss, B., Retheesh, A., Maqueda, L., Park, J.H., 2023. The European DEMO helium cooled pebble bed breeding blanket: Design status at the conclusion of the pre-concept design phase. Energies 16 (14), http://dx.doi.org/10.3390/en16145377.